Journal of Magnetic Resonance 331 (2021) 107021

Contents lists available at ScienceDirect

Journal of Magnetic Resonance

journal homepage: www.elsevier.com/locate/jmr

Low-field microwave-mediated optical hyperpolarization in optically pumped diamond

A. Ajoy [a], A. Sarkar [a], E. Druga [a], P. Zangara [b], D. Pagliero [c], C.A. Meriles [c], J.A. Reimer [d]

[a] Department of Chemistry, University of California, Berkeley, Berkeley, CA 94720, USA
[b] Universidad Nacional de Córdoba, Facultad de Matemática, Astronomía, Física y Computación, and CONICET, Instituto de Física Enrique Gaviola, X5000HUA Córdoba, Argentina
[c] Department of Physics and CUNY-Graduate Center, CUNY-City College of New York, New York, NY 10031, USA
[d] Department of Chemical and Biomolecular Engineering, and Materials Science Division Lawrence Berkeley National Laboratory, University of California, Berkeley, Berkeley, CA 94720, USA

ARTICLE INFO

Article history:
Received 9 January 2021
Revised 17 May 2021
Accepted 4 June 2021

Keywords:
Optical pumping
NV centers in diamond
Optical DNP

ABSTRACT

The emergence of a new class of optically polarizable electronic spins in diamond, nitrogen vacancy (NV) defect centers, has opened interesting new avenues for dynamic nuclear polarization. Here we review methods for the room-temperature hyperpolarization of lattice ^{13}C nuclei using optically pumped NV centers, focusing particular attention to a polarization transfer via rotating-frame level anti-crossings. We describe special features of this optical DNP mechanism at low-field, in particular, its deployability to randomly oriented diamond nanoparticles. In addition, we detail methods for indirectly obtaining high-resolution NV ESR spectra via hyperpolarization readout. These mechanistic features provide perspectives for interesting new applications exploiting the optically generated ^{13}C hyperpolarization.

1. Introduction

The nitrogen vacancy (NV) center in diamond [1–3], a spin-1 paramagnetic defect, has emerged as an attractive platform for optical dynamic nuclear polarization (DNP). It hosts a highly coherent electronic spin, with coherence times $> T_{2e} \sim 100$ns, and can be optically polarized with modest optical powers ($\lesssim 1$mW/NV/μs) even at room temperature and Earth's magnetic field [4]. NV centers can be created in the lattice through electron irradiation and annealing; the diamond host materials could either be single-crystals or nanoparticles (50 nm- 200μm in size) (see Fig. 1). The *"deployability"* of these nanodiamond particulate materials, and their high surface area (>50 m^2/g) make them compelling as DNP agents that could be harnessed for the spin polarization of molecules brought in contact with them; a broad effort is underway to realize this goal [5–12].

While the NV electrons possess excellent spin properties for DNP, they are typically present at relatively low lattice concentrations (<5 ppm), and are ill-behaved extremely close ($\lesssim 2$ nm) to the diamond surfaces. The ^{13}C nuclei in the diamond lattice, however, arise naturally at $10^4 - 10^6$ concentrations. They have long coherence times ($T_{2n}^* > 1$ms), and lifetimes ($T_{1n} \gtrsim 10$ min [13,14]), even when enriched to high concentrations. Under appropriate dynamical decoupling the rotating frame lifetimes can be extended further $T_{1\rho} > 1$s. It is attractive to consider these coherent nuclei, especially when enriched, as a relay medium to transfer polarization to external molecules tethered to the diamond surface [7,11,15].

In this paper, we review optical DNP methods for the low-field hyperpolarization of ^{13}C nuclei via NV centers; an important first step towards relayed DNP applications. Even just coaxing high optical ^{13}C polarization in diamond particles opens interesting new opportunities. The generated hyperpolarization is at optically-defined spatially resolution, can be continuously replenished, and can be generated at relatively low-cost since the need for cryogenic environments and high magnetic fields is mitigated. There are at least three complimentary mechanisms by which polarization can be induced in the ^{13}C nuclear medium, employing lab-frame or rotating frame level anti-crossings (LACs) between the electron and nuclear spins. This is accomplished exploiting *(i)* special field values $\approx$ 510G, 1020G that are natural NV-^{13}C LACs [6,16,17], or employing *(ii)* microwave sweeps [11,18] or *(iii)* field sweeps [19]. These approaches proceed via complementary mechanisms, either involving the P1 centers (substitutional Nitrogen impurities) or via directly through NV-^{13}C hyperfine couplings; each method has specific implementational advantages. In this paper, we focus particular attention to the MW-sweep mediated technique [11,18] given advantages in being completely independent of diamond crystallite orientation, allowing the hyperpolar-

https://doi.org/10.1016/j.jmr.2021.107021
1090-7807/

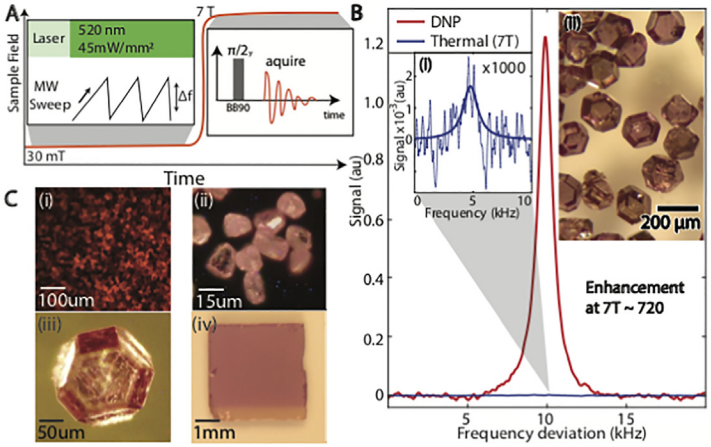

Fig. 1. Optical ^{13}C hyperpolarization in diamond. (A) DNP protocol consists of continuous laser illumination and concomitant swept microwave (MW) irradiation at low field (schematically displayed). The sample is subsequently shuttled to high field where the ^{13}C nuclear FIDs are measured. (B) *Typical hyperpolarization* in 200μm diamond powder at 36mT (red line) [23]. *Inset (i):* Thermally polarized ^{13}C NMR signal at 7T (blue line). DNP polarization is enhanced ~720 times over 7T, corresponding to a ~1% level. Polarization builds up in ~40s of optical pumping, typically limited by ^{13}C T_{1n} at the polarization field. *Inset (ii):* Microparticles employed in these measurements. (C) *Example diamond sample micrographs*, showing particles at sizes 100 nm, 10μm and 200μm, and single-crystals. DNP enhancement factors generally improve with particle size.

ization of bulk nanodiamond particles. This enables exploiting the high ^{13}C polarization levels as a resource, along with opportunities afforded by their nanoparticle form-factor [20–22].

2. Hamiltonian

DNP is predicated on special features of the NV electron, which has a Hamiltonian in a magnetic field,

$$\mathcal{H}_{\rm NV} = \Delta S_z^2 + \gamma_e \mathbf{B}_{\rm pol} \cdot \vec{S}, \tag{1}$$

where $\boldsymbol{S}$ are spin-1 Pauli operators, $\Delta = 2.87$GHz is the zero field splitting, $\mathbf{B}_{\rm pol}$ is the applied bias magnetic field at which hypeprolarization is performed ($B_{\rm pol}$ <100mT), $\hat{z}$ is the direction of the N-to-V axis in the lattice, and $\theta = \cos^{-1}(\mathbf{B}_{\rm pol}\cdot\hat{z}/B_{\rm pol})$ direction with respect to the applied field. The orientation dependence of the Hamiltonian is therefore implicit in Eq. (1). We restrict our attention here to NV centers in the negatively charged state NV$^-$. Optical pumping at modest powers (< 1mW) polarizes the NV center in $< 1\mu s$ into the $m_s = 0$ state, driven by a non-unitary process via state selective branching through a non-radiative singlet in the excited state [24]. The optically generated polarization can now be harnessed via coherent transfer to ^{13}C nuclear spin states in the pseudo two-level systems constituted by either of the $m_s = \{0, \pm 1\}$ NV manifolds [8,9].

A key advantage of the MW mediated DNP protocol is its ability to contend with the wide electronic (ESR) spectra typical of NV centers in randomly diamond particles [25,10]. Indeed, in this case, all possible orientations θ are possible in Eq. (1), manifesting in an orientationally (*inhomogeneously*) broadened NV electronic (ESR) spectrum with linewidth $\mathcal{B} > 1$ GHz even at modest fields, $B_{\rm pol}$ ~0.3T. Other DNP protocols are better conditioned to single-crystal samples [6,16,17,26]. There are then only four classes of NV center orientations (along lattice [111] directions), and the homogenous NV ESR spectral width ($\mathcal{B} \approx$10 MHz) is far narrower, determined predominantly by couplings to the ^{13}C nuclear bath and lattice crystal strain (see Fig. 3B).

NV centers couple to the lattice spin-1/2 ^{13}C nuclei via hyperfine interactions, in general represented by the tensor **A**. The Hamiltonian of the combined NV-^{13}C system then can then be written as,

$$\mathcal{H} = \mathcal{H}_{\rm NV} + \mathcal{H}_n + \mathcal{H}_{en} + \mathcal{H}_{nn}\,, \tag{2}$$

where, the nuclear Zeeman term $\mathcal{H}_n = \omega_L \sum_j I_{jz}$, and we define the Larmor frequency $\omega_L = \gamma_n B_{\rm pol}$, where $\gamma_n \approx 1.07$kHz/G is the ^{13}C magnetogyric ratio. The third term denotes the electron-nuclear hyperfine coupling, $\mathcal{H}_{en} = \sum_j \vec{S}\cdot\mathbf{A}_j\cdot\vec{I}_j$, and the strongest (first shell) interaction $A_\parallel \approx 130$MHz. The ^{13}C nuclei are in-turn dipolar coupled with one other, with the secular Hamiltonian $H_{nn} = \sum_{j<k} d_{jk}^{\rm CC}\left[3I_{zj}I_{zk} - \vec{I}_j\cdot\vec{I}_k\right]$; where the vector $z\hat{\prime}$ along $\mathbf{B}_{\rm pol}$ could, in general, differ from $\hat{z}$ in Eq. (1). The dipolar strengths $d_{jk}^{\rm CC} = \frac{\mu_0}{4\pi}\hbar\gamma_n^2(3\cos^2\theta_{jk} - 1)\frac{1}{r_{jk}^3} \sim 1$ kHz, and $\theta_{jk} = \cos^{-1}\left(\frac{\mathbf{r}_{jk}\cdot\mathbf{B}_{\rm pol}}{r_{jk}B_{\rm pol}}\right)$ is the angle of the interspin vector $\mathbf{r}_{jk}$ to the magnetic field. The median coupling strength scales $\left\langle d^{\rm CC}\right\rangle \sim \eta^{1/2}$, where η is the lattice enrichment level, easily controllable by CVD techniques [27]. Indeed, the secular Hamiltonian $\mathcal{H}_{nn}$ is a good approximation since in our hyperpolarization regime, the Larmor frequency $\omega_L > \left\langle d^{\rm CC}\right\rangle$. The ^{13}C nuclei can maintain relatively long coherence [18,28] and lifetimes [13,14] even when highly enriched. Enrichment aides in hyperpolarization relay since it leads to accelerated spin diffusion rates. Considering a simple dipolar model, the diffusion constant $D \approx \frac{\langle r_n\rangle^2}{30T_{2n}}$ [29], where the inter-nuclear spacing scales $\langle r_n\rangle \sim \eta^{-1/6}$, and taking only dipolar contributions to the linewidth $T_{2n} \approx \left\langle d^{\rm CC}\right\rangle^{-1}$; hence $D \sim \eta^{1/6}$, leading to further spin diffusion away from each NV center. Assuming an NV concentration of 1 ppm, the average inter-NV distance is $\langle r_{\rm NV}\rangle \approx$12 nm [14,30,31]; the estimated spin diffusion lengths $\sigma = \sqrt{2DT_1}$ exceed $\langle r_{\rm NV}\rangle$ past $\eta \approx 10\%$, indicating that the ^{13}C polarization can be relatively well homogenized in the lattice.

The diamond lattice also consists of P1 centers, substitutional nitrogen impurities that are spin-1/2 electronic spins but which are not optically polarizable [8]. In typical diamond crystals, P1 centers are far more numerous in the lattice compared to the NV centers, due to finite P1→ NV conversion efficiency (typical 10%). P1 centers contribute to NV and ^{13}C decoherence and relaxation, especially in high density samples where the NV center concentration is > 10ppm. The large frequency separation between these individual reservoirs, however, keeps these processes to indirect (second-order) ones [14]. In certain situations, the P1 centers can serve to accelerate ^{13}C polarization spin diffusion via four-body ^{13}C − P1 − P1 − ^{13}C flip-flops, and due to their "reach" over longer

distances in the lattice compared to direct ^{13}C interactions [32]. Simultaneously, the P1 centers can cause P1 – ^{13}C – P1 three-body flip-flop processes that can contribute to ^{13}C T1. This is, in fact, the dominant mechanism for ^{13}C relaxation at low fields [14]. Both these effects are operational simultaneously and are, in general, hard to decouple.

3. Hyperpolarization protocol

We focus first on the microwave (MW) mediated DNP protocol detailed in Fig. 1A. It proceeds through direct NV-^{13}C hyperfine interactions, and provides a key operational advantage in being independent to the lattice orientation. It entails the use of continuous laser excitation and simultaneous chirped MW irradiation (Fig. 1A); the former polarizes the NV centers, while the latter sets up coherent NV-^{13}C polarization transfer (Fig. 1A). Compared to solid-effect DNP, this mechanism presents two key differences: *(i)* There is hyperpolarization under continuous irradiation at a fixed MW frequency. *(ii)* The hyperpolarization sign is same for all parts of the spectrum, which is dependent only on the direction of the MW sweep. DNP polarization transfer efficiency is highest when conducted at low magnetic field, $B_{\rm pol} < 50$mT, due to high efficiency of the NV optical pumping, as well as the relatively benign broadening of the NV ESR spectra. At fields approaching zero field ($B_{\rm pol} < 1$mT), however, lattice polarization buildup is restricted due to low ^{13}C T_{1n}, inspite of optical pumping being highly efficient [14].

Fig. 1B shows typical hyperpolarization results, where we evaluate the generated polarization levels by shuttling the sample to a 7T detection field. Fig. 1C shows representative diamond samples that can be hyperpolarized, spanning length scales from nanoparticles to single-crystals (Fig. 1C). DNP levels are typically higher in larger particles [33–35]; nanodiamonds have larger sample damage on account of sample crushing and during electron irradiation. Recent work has indicated that these deleterious factors can be mitigated to an extent employing rapid thermal annealing (RTA) at very high temperatures [35]. RTA at 1720°C for 10 min, for instance, allowed order of magnitude gains in hyperpolarization levels in microparticles compared to standard annealing at 850°C. ESR studies revealed that this was due to a decrease in lattice paramagnetic impurities upon RTA, leading to an increase in NV T_{1e} and T_{2e}, as well as ^{13}C T_{1n}.

Technical requirements for ^{13}C hyperpolarization via Fig. 1A are modest [23]. We estimate, for example, an optical and MW power of 1μW and 1nW respectively for the polarization of a single 1μm particles. Moreover, the MW sweep rates are slow, typically ($\omega_r < 1$kHz), determined by the NV center T_{1e} at the low illumination rates. DNP can be accomplished even under large $\mathbf{B}_{\rm pol}$ field inhomogeneities. These features portend development of inexpensive and portable benchtop devices for the rapid generation of ^{13}C polarization in diamonds [23].

4. Landau–Zener polarization transfer

Mechanistically, polarization transfer arises from setting up Landau–Zener (LZ) anticrossings in the rotating frame of the chirped microwaves. We present here a toy-model that uncovers this physics, considering simple cases of an NV center coupled to one and two ^{13}C nuclei respectively (see Fig. 2). We consider direct NV$\rightarrow$ ^{13}C hyperpolarization processes, neglecting the effect of internuclear coupling and hence spin diffusion. The origin of hyperpolarization can be traced to bias resulting from differential traversals of LZ system conditioned on the starting nuclear spin state. Due to optical pumping, we start with the nuclear spins unpolarized, but restricted to the $m_s = 0$ manifold; i.e. with equal populations in $\{|0,\uparrow\rangle, |0,\downarrow\rangle\}$ states. As we elucidate below, traversals through the LZ system in Fig. 2 occur in a manner that the nuclear populations follow:

$$P_+(|\downarrow\rangle) \approx P_-(|\downarrow\rangle)\,;\, P_+(|\uparrow\rangle) = (1-\varepsilon)P_-(|\uparrow\rangle) + \varepsilon P_-(|\downarrow\rangle), \tag{3}$$

where $P_-(\cdot)$ and $P_+(\cdot)$ refer to nuclear populations before and after the LZ crossing. Indeed, one of the nuclear states is unaffected, while the other is flipped with a finite probability ε. Successive sweeps through the LZ system then set up a "*ratchet*" that builds hyperpolarization in the $|\downarrow\rangle$ state. The factor ε in Eq. (3) also characterizes the DNP efficiency, typically $\varepsilon \sim 0.1$–5% [11]. In practical terms, the number of such polarization transfer sweep events N_s are determined by the MW repetition rate ω_r to maintain sweep adiabaticity constraints, the NV repolarization rate, and the overall nuclear T_{1n}. In our experiments, $N_s \approx \omega_r T_{1n} = 10^4$ traversals are typical.

To elaborate on the spin physics underlying Eq. (3), consider the Hamiltonian of an NV-^{13}C system, considering the general case of N nuclear spins coupled to the NV center with hyperfine strength A_j. Fig. 2 shows representative cases of $N = 1$ and $N = 2$ nuclei respectively. We assume operation at low-field conditions $B_{\rm pol} < 100$mT, such that $\omega_L < |A_j|$ (energy levels shown in inset of Fig. 2A). In Fig. 2 we restrict ourselves to the $m_s = \{0, +1\}$ NV manifold, and assume for simplicity that the NV axis is aligned with $\mathbf{B}_{\rm pol}$. The effective nuclear quantization is conditioned on the exact NV manifold: *(i)* the $m_s = 0$ state is non-magnetic; hence the nuclear spins are quantized here in Zeeman field $\mathbf{B}_{\rm pol}$ with frequency ω_L. There is additionally a second order correction mediated by the hyperfine term, leading to an effective nuclear frequency $\omega_j^{(0)} \approx \omega_L + \frac{\gamma_e B_{\rm pol} A_{j,\perp}}{\Delta}$ [36]. *(ii)* In the $m_s = +1$ manifold, on the other hand, there is combined action of the Zeeman field and the NV hyperfine coupling, $\omega_j^{(1)} = \sqrt{(\omega_L + A_{j,\parallel})^2 + A_{j,\perp}^2}$. Indeed, the effective quantization axis $\hat{z}_j$ in this case need not be coincident with $\mathbf{B}_{\rm pol}$; in general, $\hat{z}_j = \hat{z}\cos\phi_j + \hat{x}\sin\phi_j$, and the angle $\phi_j = \tan^{-1}\left[A_{j,\perp}/(\omega_L + A_{j,\parallel})\right]$. In our operational low-field regime, the frequency $\omega_j^{(1)} > \omega_j^{(0)}$. Let us assume linear MW chirps applied to the system with electron Rabi frequency Ω_e, and a sweep repetition rate ω_r. In this case, the instantaneous MW frequency $\omega_{\rm MW}(t) = \mathcal{B}\omega_r t + \omega_s$, where $\mathcal{B}$ is the sweep bandwidth, and the starting frequency, $\omega_s = (\Delta + \gamma_e B_{\rm pol}) - \mathcal{B}/2$. The system Hamiltonian in the rotating frame is then,

$$\mathcal{H} = (\Delta - \omega_{\rm MW})S_z^2 + \gamma_e B_{\rm pol} S_z + \Omega_e S_x + \sum_{j=1}^{N}\left[\omega_j^{(0)}\mathcal{P}_0 I_{zj} + \omega_j^{(1)}\mathcal{P}_1 I_{zj}\right] \tag{4}$$

where in the electron basis of $m_s = \{0, +1\}$ manifolds, $\mathcal{P}_0 = \begin{pmatrix} 1 & 0 \\ 0 & 0 \end{pmatrix} \otimes \mathbf{1}_N$; $\mathcal{P}_1 = \begin{pmatrix} 0 & 0 \\ 0 & 1 \end{pmatrix} \otimes \mathbf{1}_N$, are respective projection operators, and without loss of generality, $I_{zj} = I_{zj}\cos\phi_j + I_{xj}\sin\phi_j$. We separate $\mathcal{H} = \mathcal{H}_{\rm sec} + \mathcal{H}_{\rm non-sec}$ into its secular and non-secular parts with respect to $\hat{z}$. The inset in Fig. 2A shows the corresponding secular energy levels. The off-diagonal terms stem from $\{A_{j,\perp}, \Omega_e\}$ contributions. As a function of frequency offset $\delta\omega_{\rm MW} = (\Delta + \gamma_e B_{\rm pol} - \omega_{\rm MW})$, this gives rise to the anti-crossing diagram as indicated by the solid lines in Fig. 2A; we label the levels on either side by their secular eigenstates. To physically interpret the LACs and the resulting energy gaps, let us first consider the situation with $A_\perp = 0$ (dashed lines in Fig. 2A). There is then a single LAC, between levels $|0,\downarrow\rangle \leftrightarrow |+1,\downarrow\rangle$, and corresponding to an electron flip, similar to the situation encountered under an NV rapid adiabatic passage; the energy gap is therefore $g_1 = \Omega_e$.

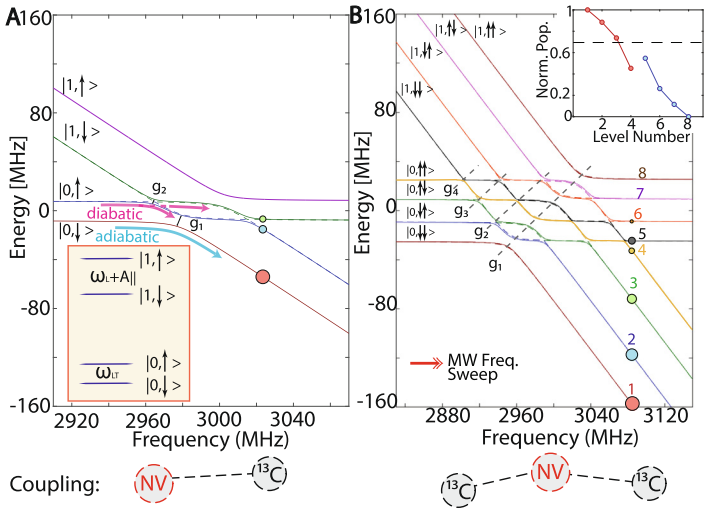

Fig. 2. DNP mechanism. (A)*Landau–Zener anticrossings* in the rotating frame with assumed Rabi frequency Ω_e, and $A_\perp = A_\parallel$. We assume applied low-to-high frequency sweeps, starting with an initial unpolarized nuclear state in the $m_s = 0$ manifold. *Inset* shows lab frame energy levels for a NV-^{13}C system, restricted to the $m_s = \{0, +1\}$ manifolds. We assume to work at low-fields wherein nuclear Larmor frequency $\omega_L < A_\parallel$. Dashed lines indicate the crossings assuming $A_\perp = 0$. The two LZ energy gaps $\{g_1, g_2\}$ conditioned the nuclear spin states $|\downarrow\rangle$ and $|\uparrow\rangle$, are large and small respectively, leading to adiabatic and diabatic transitions upon traversals through the LAC system (blue and red lines). This leads to population bias in the lower branch (balls show populations) and ^{13}C hyperpolarization in nuclear state $|\downarrow\rangle$ upon NV repolarization. (B) *System with two* ^{13}C *nuclei* coupled to an NV center. In this toy model, we assume effective nuclear frequencies for the two nuclei $\omega_j^{(0,1)}$ in the $m_s = \{0, 1\}$ manifold such that $\omega_j^{(0)} = 2j^p; \omega_j^{(1)} = 5j^p$, where $p = 1.1$. There are multiple LZ anticrossings, and a hierarchy of energy gaps $(g_1 - g_4)$ are successively traversed upon a low-to-high frequency sweep. Time evolution starting with an nuclear unpolarized state leads to system bias and hyperpolarization in the lower two levels energy levels (*inset*).

Now considering the situation with finite $A_\perp$ results in two energy gaps, as indicated in Fig. 2A. The gap g_2 arises from a double electron-nuclear spin flip $|0, \uparrow\rangle \leftrightarrow |+1, \downarrow\rangle$, and is hence smaller. Traversing the LAC system is hence nuclear state selective: at an appropriately chosen MW chirp rate $\dot{\omega} = \mathcal{B}\omega_r$, such that $\dot{\omega} g_1^{-2} \ll 1$ and $\dot{\omega} g_2^{-2} \gtrsim 1$, one can arrange to be *adiabatic* with respect to g_1 but *diabatic* respect to g_2. Starting with equal populations in the two nuclear states therefore leads to population bifurcating on the nuclear spin starting from state $|0, \uparrow\rangle$. This is shown schematically by the balls in Fig. 2A that represent the corresponding nuclear populations. The transition probability following Eq. (3) is then, $\varepsilon \sim \exp(-g_2^2/\dot{\omega})$. This differential traversal sets up bias in the system that ultimately drives the ratchet-like NV-^{13}C hyperpolarization transfer. Upon optical NV repolarization, the states $|+1, \downarrow\rangle \rightarrow |0, \downarrow\rangle$ are polarized to $m_s = 0$ manifold, leading to nuclear polarization buildup in state $|\downarrow\rangle$. Another consequence is that the bias is MW sweep-direction dependent; sweeping the MWs from high-to-low frequency in Fig. 2A inverts the sequence of energy gaps encountered during the sweep, and causes hyperpolarization in the opposite nuclear spin state ($|\uparrow\rangle$). Polarization is ultimately determined as an interplay of the polarization transfer efficiency per microwave (MW) sweep event, and the total number of sweeps that can be carried out per second. Intuitively, polarization can be transferred more rapidly if the ratchet is operated faster (higher $\dot{\omega}$), but this comes at the cost of lower efficiency *per* sweep since the hierarchy $g_2^2 \lesssim \dot{\omega} \ll g_1^2$ is then effected. We have previously experimentally measured a polarization transfer efficiency of $\sim$10% for an enriched ^{13}C sample [11].

Even this simplistic picture suggests that for obtaining the spin-ratchet as in Eq. (3), both the MW repetition rates ω_r as well as the laser power have to be sufficiently low: the former due to requirements of adiabaticity in the sweeps through the anti-crossing region, and the latter so that the NV repolarization is sufficiently slow so as not to break coherence during the LZ traversal. Indeed, we find experimentally that at the laser power levels we typically employ in these experiments, the NV repolarization rate is approximately $(T_{1e})^{-1}$. The latter also bottlenecks the polarization buildup, in practical scenarios we also have $\omega_r \approx (T_{1e})^{-1}$ [23].

Fig. 2B elucidates a similar situation of an NV center coupled to *two* ^{13}C nuclei, and ignoring their internuclear dipolar coupling. For simplicity, we assume a toy-model to illustrate the physics, choosing nuclear frequencies $\omega_j^{(0)} = 2j^p$ and $\omega_j^{(1)} = 5j^p$ in the $m_s = \{0, 1\}$ manifolds, where $p = 1.1$. We further assume that $A_{j,\perp} = A_{j,\parallel}$, or in effect, $\phi_j = \pi/4$. The levels in the inset of Fig. 2B are once again are labeled by secular eigenstates. Considering the LZ crossings in Fig. 2B, a series of energy gaps is again evident $(g_1 - g_4)$; traversal through the LZ system leads to a successive encounters through a different number of LACs conditional on the starting nuclear state. The energy gaps themselves are mirror-symmetric with respect to the center of the LZ diagram, and have a hierarchy related to the total number of spin-flips involved (see Fig. 2B). Importantly, higher levels in diagram, corresponding to the anti-polarized nuclear manifold, undergo a larger number of population bifurcations through the LAC system compared to the lower manifold. There is hence an overall bias in the system tending to the right and bottom in the LZ system in Fig. 2B, indicated by the arrows; ultimately leading to hyperpolarization buildup in nuclear state $|\downarrow\downarrow\rangle$ (balls in Fig. 2B). The inset in Fig. 2B indicates the final net populations in each of the levels (labeled 1–8 in Fig. 2B) assuming one starts from a purely mixed state on the nuclear spins.

In some respects, the mechanisms in Fig. 2 shares similarities with integrated solid effect (ISE) employed in the context of DNP in photoexcited triplet systems [37–39]. However, we comment on some key points of difference. *(i)* ISE is typically performed at elevated magnetic fields $B_{\text{pol}} > 0.5$T, wherein the nuclear Larmor frequency ω_L exceeds the average hyperfine coupling $\omega_L \gg |A|$. In contrast, the DNP above mechanism operates at the low-field, where this hierarchy is inverted. *(ii)* With respect to the rotating frame LACs, the hierarchy of energy gaps (Fig. 2A,B) naturally result in adiabatic or diabatic traversals conditioned on the starting nuclear states. Hyperpolarization arises because these hierarchical gaps are encountered in a particular sequence, as opposed to ISE.

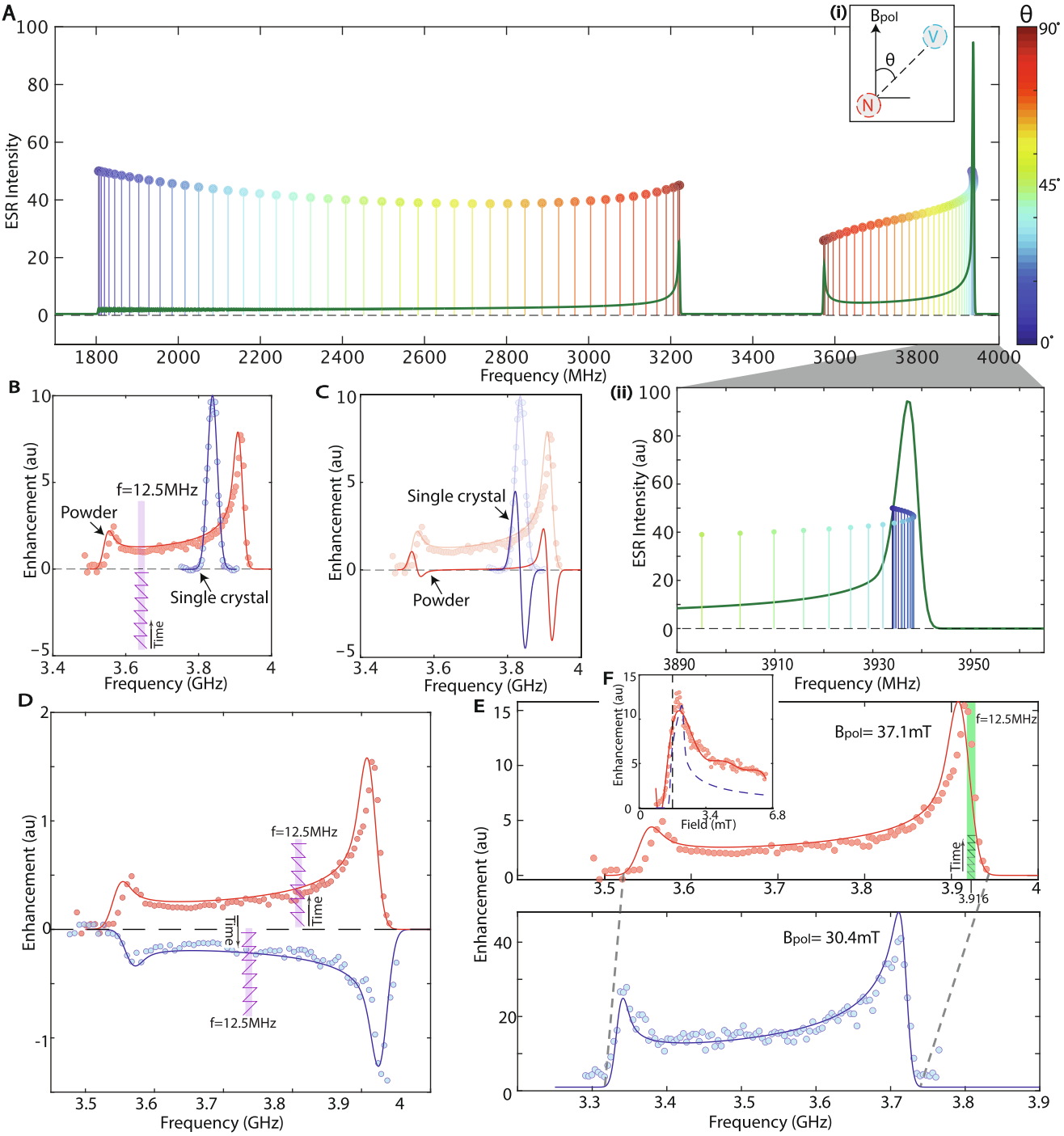

Fig. 3. Orientation independence of ^{13}C hyperpolarization revealed via DNP-maps of the NV ESR spectrum. (A) Model of the orientationally broadened NV ESR spectrum in the $m_s = \pm 1$ manifold (green line) at $B_{pol} = 38$ mT. The vertical bars display the frequency position of NV center orientations (*Inset (i)*) at $\Delta\theta = 5^\circ$ intervals; colors represent θ values. The $m_s = +1$ manifold is narrower and with a greater concentration of levels per frequency bandwidth compared to the $m_s = -1$ manifold. *Inset (ii)*: Zoom into the $m_s = +1$ manifold, shows the concentration of NV ESR spectral lines corresponding to a $\Delta\theta \approx 30^\circ$ orientational cone. Efficient DNP can hence be excited just via MW sweeps over the narrow $\Delta f \approx 50$ MHz region (shaded). (B) *DNP mediated mapping of NV ESR spectrum*. We consider positive MW sweeps in the $m_s = +1$ manifold at ~37.1mT carried out over narrow $\Delta f = 12.5$ MHz windows, whose center frequency is varied. The ^{13}C NMR signal then faithfully reflects the underlying NV density of states and corresponding EPR spectrum (fits are solid lines to the model in A). Blue line and points are for a similar experiment on a single-crystal (with NV axes at $\theta = 54.7^\circ$ to $\mathbf{B}_{pol}$). (C) *Spectral derivative* calculated from the ESR spectra, showing that hyperpolarization intensities do not change much with orientation except for two frequency windows at the extrema of the spectrum. (D) *Positive and negative MW sweeps* lead to a sign inversion of the DNP signal from every part of the NV ESR spectrum. (E) *DNP under changing field*. With increasing field (legend), the hyperpolarization mapped ESR spectra widen and have their centroid move to high frequency as predicted. Dashed lines denote corresponding 0° and 90° orientations. (F) In a complementary experiment, here the MW sweep is fixed in a $\Delta f = 12.5$ MHz bandwidth about $f = 3.916$ GHz (shaded region in E), and the magnetic field is varied. The ^{13}C DNP profiles once again reflect the NV center density of states as modeled in (A).

5. Orientational independence

This MW protocol is agnostic to the exact orientation of the diamond particle with respect to $\mathbf{B}_{pol}$. The green line in Fig. 3A describes the simulated NV ESR spectrum in the $m_s = \pm 1$ manifold for randomly oriented powder including all orientations of $\theta \in [0, \pi/2]$ (Fig. 3A(i)) at $B_{pol} = 38$ mT. Vertical bars in Fig. 3A denote the positions of ESR transitions corresponding to θ values

spaced apart by 5° (colors). The heights of the bars denote the respective transition intensities $\mathcal{T}(\theta, B_{\rm pol})$, calculated by diagonalizing the Hamiltonian $\mathcal{H}_{\rm NV}$ in Eq. (1). To a good approximation, it is sufficient to consider the Hamiltonian of the NV center alone, ignoring the ^{13}C nuclei. Instead, they are just assumed to contribute to the homogeneous ESR linewidth $\mathcal{B}$ for every orientation. From the eigenvectors $\mathcal{H}_{\rm NV}|v_k\rangle = E_k|v_k\rangle$, we calculate the transition intensities [23] as $\mathcal{T}(\theta, B_{\rm pol}) \sim \sum_{k<\ell}\sum_m |\langle v_k \mid S_m \mid v_\ell\rangle|^2 [\langle v_k \mid \rho \mid v_k\rangle - \langle v_\ell \mid \rho \mid v_\ell\rangle]$, where S are spin-1 Pauli matrices, and $m \in \{x, y, z\}$. The first factor quantifies the transition probability, and the second factor describes the population difference between the eigenstates, with $\rho = \mathbb{1} - S_z^2/3$. To construct the inhomogenously broadend spectrum (green line) in Fig. 3A, we assume the individual $\mathcal{T}(\theta)$ spectra have a Gaussian width $\mathcal{B} \approx 10$G. The extremities of the spectra at low fields are easy to identify, and correspond to the aligned ($\theta = 0°$), and perpendicular orientations ($\theta = 90°$) respectively with respect to $\mathbf{B}_{\rm pol}$. The frequency locations occur, in the $m_s = \mp 1$ manifolds, at $f_0^{\mp 1} = \Delta \mp \gamma_e B_{\rm pol}$ for aligned orientations, and at $f_{90}^{\mp 1} = \frac{1}{2}\left[\Delta + \sqrt{\Delta^2 + (2\gamma_e B_{\rm pol})^2}\right]$ and $\left[\sqrt{\Delta^2 + (2\gamma_e B_{\rm pol})^2}\right]$ for the perpendicular orientations.

Two comments are in order: *(i)* The $m_s = -1$ branch encloses a broad inhomogeneous linewidth, >1 GHz even at moderate fields $B_{\rm pol} > 20$mT. The components corresponding to different orientations are approximately uniformly spaced apart, evident in the bars in Fig. 3A (see also Fig. 3C). In the narrower $m_s = +1$ branch, on the other hand, there is a nonlinear bunching of frequencies corresponding to different θ orientations. This is represented in the zoomed in inset in Fig. 3A(ii). A large cone of orientations ($\Delta\theta = 30°$) occupy the narrow $\mathcal{B} \approx 50$ MHz bandwidth at the edge of the spectrum. *(ii)* The high concentration of electronic density of states makes the $m_s = +1$ branch particularly attractive for optimizing hyperpolarization levels. Since every particle has NV centers with four different orientations, with a high probability every crystallite has at least one NV center in the Δf cone; allowing efficient ^{13}C hyperpolarization of the powder with just narrow bandwidth MW sweeps.

While simplifying approximations have gone into the evaluation of Fig. 3A, they are borne out by experiments. In Fig. 3B, we carry out DNP using swept MWs in a small frequency window (here $\Delta f = 10$ MHz), whose center is moved across $m_s = +1$ branch in Fig. 3A. We plot the obtained ^{13}C NMR hyperpolarization intensities (points in Fig. 3B); as is evident, they faithfully track underlying ESR spectrum (solid line). We fit the ESR spectrum here with a single free parameter ($B_{\rm pol} = 37.2$ mT). For comparison, we carry out similar experiments on a single-crystal sample (blue line in Fig. 3B) with the magnetic field $\mathbf{B}_{\rm pol}$ aligned along the [100] axis, *i.e.* with $\theta = 54°$. In this symmetry orientation, the four NV center families have overlapping frequency positions, resulting in a homogenous Gaussian ESR spectrum, dominated by strain and hyperfine couplings ^{13}C nuclei. Fig. 3B therefore visually elucidates the NV ESR spectral differences in a single-crystal and powder.

The solid lines in Fig. 3C describe the spectral derivative, showing that even in a powder, the hyperpolarization signal (and hence electronic density of states) remains approximately constant except for at the edges of the spectrum. Fig. 3D shows the experimental ESR maps in the $m_s = +1$ manifold taken at two different magnetic fields (37.1mT, 30.4mT), demonstrating that the spectrum widens and its centroid moves as expected. Dashed lines indicate the 0° and 90° orientations for clarity. Fig. 3E considers a complementary experiment, wherein the MW sweeps are fixed in a small 12.5 MHz window at the end of the spectrum, and the magnetic field is scanned. Once again, the hyperpolarization signal closely reflects the underlying ESR spectrum; the dashed line is a fit to the prediction from Fig. 3A.

Finally, in Fig. 3F we consider the effect of the MW sweep direction to the DNP signal (see Fig. 2). A similar experiment to Fig. 3B is performed with $\Delta f = 10$ MHz windows but now with MWs with low-to-high (red) and high-to-low (blue) sweep directions. As evident, the hyperpolarization sign only depends on the direction of the MW sweep, but is identical for all parts of the ESR spectrum. The latter exemplifies consequences of the mechanistic difference with respect to more traditional (high-field) DNP techniques.

6. "Hole burning DNP spectroscopy

While the hyperpolarization levels reflect the cumulative underlying ESR spectrum being swept over (Fig. 3), obtaining high resolution DNP-ESR spectra by reducing the sweep window to the limit $\Delta f \to 0$ is not straightforward. *(i)* There is firstly a loss of signal intensity because only a narrow part of the electronic density of states is being swept over. *(ii)* Moreover, the LZ DNP mechanism laid out in Fig. 2 becomes ineffective when $\Delta f \to 0$ since the conditions for adiabatic traversals assume that the MW sweeps occur from far off-resonance limits on either side of the LAC system. *(iii)* The ratchet-like mechanism in Fig. 2 assumes that NV repolarization under laser excitation occurs far away from the LAC regions; this too is a poor approximation as $\Delta f \to 0$. *(iv)* Finally, MW frequency chirps in a small range are often sensitive to phase noise artifacts that broaden the effective chirp window, ultimately limiting frequency resolution attainable. This is especially true for Δf<100 kHz windows and when the MW chirps are created with voltage controlled oscillator (VCO) sources, like the ones we employ for experiments in Fig. 3.

To address these challenges in the $\Delta f \to 0$ limit, we construct a new *"hole burning"* DNP strategy as in Fig. 4, employing dual-MW excitation on the NVs. Consider, for simplicity, an inhomogeneously broadened NV center ESR spectrum with linewidth $\mathcal{B}$ typical for that arising from random orientations. Fig. 4A-B schematically lays out the approach; MWs are produced from two sources: *(i)* one, a wide bandwidth MW chirp across the NV ESR spectrum with a *fixed* sweep bandwidth $\Delta f_{\rm chirp} \geqslant \mathcal{B}$, and *(ii)* second, a narrow single frequency MW tone of f_{ac}, which is scanned across the spectrum. As Fig. 4B indicates, the single tone MW excites the resonant NV electrons, and saturates their populations in the $m_s = \{0, +1\}$ levels. As a result, polarization transfer previously driven by $\Delta f_{\rm chirp}$ is hindered selectively these NV electrons. As the tone f_{ac} (blue line in Fig. 4B) can now swept be over in frequency space, one obtains an indirectly mapped ESR spectrum (with negative contrast), but with higher resolution and contrast than possible via narrow bandwidth MW sweeps alone. The signal contrast obtained is proportional to the f_{ac} MW tone power as well as the underlying ESR transition intensity.

Fig. 4C-D demonstrates proof-of-concept experiments on a misorientated single-crystal diamond sample, which we choose because the sharp (narrow) ESR spectra makes a demonstration of the effect easier. Indeed, scanning the f_{ac} frequency reveals the high resolution "hole-burnt" ESR spectra showing the four NV center families. The contrast obtained with alternate MW sweep directions is opposite with respect to employing the MW sweeps alone as in Fig. 3B. We note that these experiments are performed with a low-cost VCO source to produce the swept MWs $\Delta f_{\rm chirp}$; it has a intrinsically high phase noise (≈-70dBc/Hz). Yet, the hole-burnt spectra reveals the two underlying NV center families, here at a higher resolution than possible via swept MWs alone. More details of the ultimate spectral resolutions experimentally obtainable

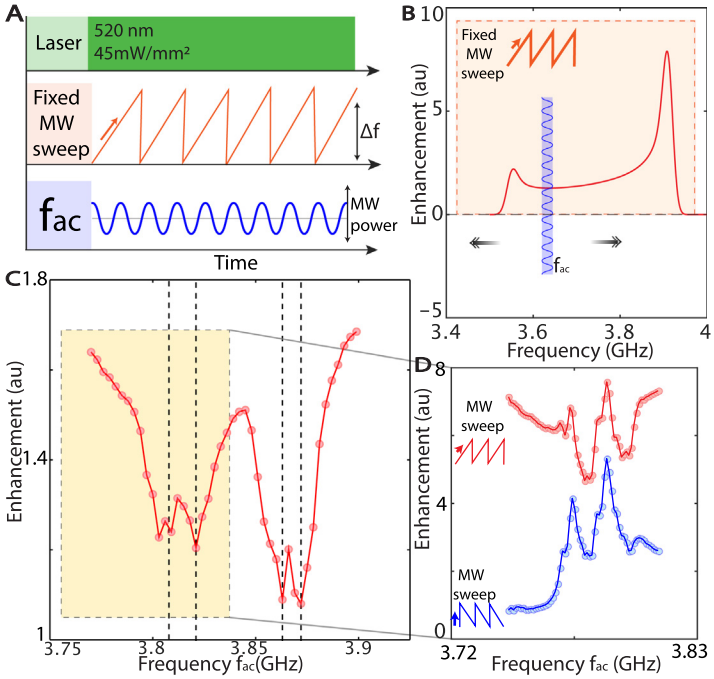

Fig. 4. "Hole burning" DNP experiments to unravel homogeneously broadened NV center spectra. (A) *Protocol* consists of MW chirps are applied over a wide (fixed) bandwidth Δf (orange) and a single MW tone at frequency f_{ac} (blue). (B) *Principle:* Consider an NV ESR spectrum (red), and applied MW chirp over the wide bandwidth (orange). Now, for the NV centers resonant with the tone f_{ac} (blue), there is a saturation of the NV population, and hence loss of ^{13}C hyperpolarization transferred via the swept MWs. Upon varying tone frequency f_{ac}, this manifests as a "hole" in the obtained DNP spectrum at NV center resonance, therefore unraveling with high contrast the NV EPR spectrum. (C) *Hole-burnt DNP* carried out on a single crystal sample with varying f_{ac} reveals the four underlying NV center orientations (dashed lines) constituting an originally broad DNP profile. (D) *Zoom in* to the two NV families on the left (shaded in C) via hole-burning DNP, with chirped MWs applied with low-to-high or high-to-low frequency. Hole burned spectra manifest with opposite sign than those in Fig. 3.

through this approach, and with accompanying high-resolution ESR spectra will be presented in a forthcoming manuscript.

7. Discussion

DNP methodologies with NV centers in diamond naturally operate at low magnetic fields and room temperature, a regime inaccessible in traditional DNP approaches. There is here an inversion in the hierarchy in the Hamiltonians; hyperfine couplings between the electron and nuclear spins, typically a perturbation respect to the nuclear Larmor frequency at high-field, can now be sizably large in comparison, $\omega_L < |A|$. These features allow interesting means to setup electron-nuclear LACs in either the laboratory frame or the rotating frame to drive the DNP process; polarization transfer proceeding either directly as an electron-nuclear process from the optically polarizable electrons, or as a many electron-nuclear process involving additional (unpolarized) paramagnetic spins. In addition to these interesting new mechanistic features, we note more broadly that optical DNP methods offer fundamental technological advantages [23]. This includes *(i)* room temperature operation without the requirement for cryogenics, *(ii)* optical replenishability, and *(iii)* possibilities for compact hyperpolarizer devices due to convenience of laser-based optical excitation and 2-4 GHz (S-band) MW irradiation at low-fields.

Finally, optical DNP in nanoparticle media allow opportunities for the deployment of hyperpolarization sources into materials of interest. Indeed the nanodiamonds can be physically transported, and excited remotely through a laser. Transferring the polarization to analytes outside diamond is an exciting thrust area but still fraught with challenges, primarily associated with creating pristine diamond surfaces free of paramagnetics such that surface ^{13}C T_{1n} times remain high. That said, ^{13}C hyperpolarization in the diamond itself can open interesting new avenues in quantum sensing and imaging [40–42], wherein nanodiamonds can be imaged through in dual-modes of optics and MRI simultaneously with advantages of background suppression and relative immunity to optical scattering.

8. Conclusion

In this manuscript, we have reviewed special features of dynamic nuclear polarization via optically pumped NV centers in diamond. The mechanism of electron-nuclear polarization transfer is qualitatively different due to access to the novel new hyperpolarization regimes at low-field and room temperature, and wherein traditional (high-field) Hamiltonian hierarchies are inverted. The generated hyperpolarization is diamond crystallite orientation independent, and also indirectly reports on the underlying electronic spectrum, allowing new methodologies for DNP mediated ESR spectroscopy. These mechanistic features give rise to exciting new avenues for exploiting optical hyperpolarization, both fundamental as well as technological.

This work is funded by NSF under GOALI 1903803 and ONR under N00014-20-1-2806.

Declaration of Competing Interest

The authors declare that they have no known competing financial interests or personal relationships that could have appeared to influence the work reported in this paper.

References

[1] A. Lenef, S.W. Brown, D.A. Redman, S.C. Rand, J. Shigley, E. Fritsch, Electronic structure of the n-v center in diamond: Experiments, Phys. Rev. B 53 (1996) 13427.

[2] F. Jelezko, J. Wrachtrup, Single defect centres in diamond: A review, Phys. Status Solidi (A) 203 (2006) 3207.

[3] N.B. Manson, J.P. Harrison, M.J. Sellars, Nitrogen-vacancy center in diamond: Model of the electronic structure and associated dynamics, Phys. Rev. B 74 (2006) 104303.
[4] P. Neumann, R. Kolesov, V. Jacques, J. Beck, J. Tisler, A. Batalov, L. Rogers, N.B. Manson, G. Balasubramanian, F. Jelezko, J. Wrachtrup, Excited-state spectroscopy of single nv defects in diamond using optically detected magnetic resonance, New J. Phys. 11 (2009) 013017, 10 pp.
[5] V. Jacques, P. Neumann, J. Beck, M. Markham, D. Twitchen, J. Meijer, F. Kaiser, G. Balasubramanian, F. Jelezko, J. Wrachtrup, Dynamic polarization of single nuclear spins by optical pumping of nitrogen-vacancy color centers in diamond at room temperature, Phys. Rev. Lett. 102 (2009) 057403.
[6] R. Fischer, C.O. Bretschneider, P. London, D. Budker, D. Gershoni, L. Frydman, Bulk nuclear polarization enhanced at room temperature by optical pumping, Phys. Rev. Lett. 111 (2013) 057601.
[7] D. Abrams, M.E. Trusheim, D.R. Englund, M.D. Shattuck, C.A. Meriles, Dynamic nuclear spin polarization of liquids and gases in contact with nanostructured diamond, Nano Lett. 14 (2014) 2471.
[8] C. Belthangady, N. Bar-Gill, L.M. Pham, K. Arai, D. Le Sage, P. Cappellaro, R.L. Walsworth, Dressed-state resonant coupling between bright and dark spins in diamond, Phys. Rev. Lett. 110 (2013) 157601.
[9] P. London, J. Scheuer, J.-M. Cai, I. Schwarz, A. Retzker, M. Plenio, M. Katagiri, T. Teraji, S. Koizumi, J. Isoya, et al., Detecting and polarizing nuclear spins with double resonance on a single electron spin, Phys. Rev. Lett. 111 (2013) 067601.
[10] Q. Chen, I. Schwarz, F. Jelezko, A. Retzker, M. Plenio, Optical hyperpolarization of c 13 nuclear spins in nanodiamond ensembles, Phys. Rev. B 92 (2015) 184420.
[11] A. Ajoy, K. Liu, R. Nazaryan, X. Lv, P.R. Zangara, B. Safvati, G. Wang, D. Arnold, G. Li, A. Lin, et al., Orientation-independent room temperature optical 13c hyperpolarization in powdered diamond, Sci. Adv. 4 (2018a) eaar5492.
[12] I. Schwartz, J. Scheuer, B. Tratzmiller, S. Müller, Q. Chen, I. Dhand, Z.-Y. Wang, C. Müller, B. Naydenov, F. Jelezko, et al., Robust optical polarization of nuclear spin baths using hamiltonian engineering of nitrogen-vacancy center quantum dynamics, Sci. Adv. 4 (2018) eaat8978.
[13] E. Rej, T. Gaebel, T. Boele, D.E. Waddington, D.J. Reilly, Hyperpolarized nanodiamond with long spin-relaxation times, Nat. Commun. 6 (2015).
[14] A. Ajoy, B. Safvati, R. Nazaryan, J. Oon, B. Han, P. Raghavan, R. Nirodi, A. Aguilar, K. Liu, X. Cai, et al., Hyperpolarized relaxometry based nuclear t 1 noise spectroscopy in diamond, Nat. Commun. 10 (2019) 1.
[15] J.-P. Tetienne, L. Hall, A. Healey, G. White, M.-A. Sani, F. Separovic, and L. Hollenberg, Prospects for nuclear spin hyperpolarisation of molecular samples using nitrogen-vacancy centres in diamond, noop arXiv preprint arXiv:2008.12417 (2020).
[16] D. Pagliero, K.K. Rao, P.R. Zangara, S. Dhomkar, H.H. Wong, A. Abril, N. Aslam, A. Parker, J. King, C.E. Avalos, et al., Multispin-assisted optical pumping of bulk c 13 nuclear spin polarization in diamond, Phys. Rev. B 97 (2018) 024422.
[17] R. Wunderlich, J. Kohlrautz, B. Abel, J. Haase, J. Meijer, Optically induced cross relaxation via nitrogen-related defects for bulk diamond c 13 hyperpolarization, Phys. Rev. B 96 (2017) 220407.
[18] A. Ajoy, R. Nazaryan, K. Liu, X. Lv, B. Safvati, G. Wang, E. Druga, J. Reimer, D. Suter, C. Ramanathan, et al., Enhanced dynamic nuclear polarization via swept microwave frequency combs, Proc. Nat. Acad. Sci. 115 (2018) 10576.
[19] J. Henshaw, D. Pagliero, P.R. Zangara, M.B. Franzoni, A. Ajoy, R.H. Acosta, J.A. Reimer, A. Pines, C.A. Meriles, Carbon-13 dynamic nuclear polarization in diamond via a microwave-free integrated cross effect, Proc. Nat. Acad. Sci. 116 (2019) 18334.
[20] A.M. Schrand, S.A.C. Hens, O.A. Shenderova, Nanodiamond particles: properties and perspectives for bioapplications, Critical Rev. Solid State Materials Sci. 34 (2009) 18.
[21] M. Baidakova et al., New prospects and frontiers of nanodiamond clusters, J. Phys. D: Appl. Phys. 40 (2007) 6300.
[22] M. Chipaux, K.J. van der Laan, S.R. Hemelaar, M. Hasani, T. Zheng, R. Schirhagl, Nanodiamonds and their applications in cells, Small 14 (2018) 1704263.
[23] A. Ajoy, R. Nazaryan, E. Druga, K. Liu, A. Aguilar, B. Han, M. Gierth, J.T. Oon, B. Safvati, R. Tsang, et al., Room temperature optical nanodiamond hyperpolarizer: Physics, design, and operation, noop, Rev. Sci. Instrum. 91 (2020) 023106.
[24] M.W. Doherty, N.B. Manson, P. Delaney, L.C.L. Hollenberg, The negatively charged nitrogen-vacancy centre in diamond: the electronic solution, New J. Phys. 13 (2011) 025019.
[25] K. Jeong, A.J. Parker, R.H. Page, A. Pines, C.C. Vassiliou, J.P. King, Understanding the magnetic resonance spectrum of nitrogen vacancy centers in an ensemble of randomly oriented nanodiamonds, noop, J. Phys. Chem. C 121 (2017) 21057.
[26] J. Scheuer, I. Schwartz, Q. Chen, D. Schulze-Sünninghausen, P. Carl, P. Höfer, A. Retzker, H. Sumiya, J. Isoya, B. Luy, et al., Optically induced dynamic nuclear spin polarisation in diamond, New J. Phys. 18 (2016) 013040.
[27] T. Anthony, J. Fleischer, J. Olson, D.G. Cahill, The thermal conductivity of isotopically enriched polycrystalline diamond films, J. Appl. Phys. 69 (1991) 8122.
[28] A. Ajoy, R. Nirodi, A. Sarkar, P. Reshetikhin, E. Druga, A. Akkiraju, M. McAllister, G. Maineri, S. Le, A. Lin, et al., Dynamical decoupling in interacting systems: applications to signal-enhanced hyperpolarized readout, arXiv preprint arXiv:2008.08323 (2020b).
[29] A. Abragam, Principles of Nuclear Magnetism, Oxford Univ. Press, 1961.
[30] E. Reynhardt, C. Terblanche, 13c relaxation in natural diamond, Chem. Phys. Lett. 269 (1997) 464.
[31] E. Reynhardt, Spin lattice relaxation of spin-nuclei in solids containing diluted paramagnetic impurity centers. i. zeeman polarization of nuclear spin system, Concepts Magnetic Resonance Part A 19A (2003) 20.
[32] D. Pagliero, P.R. Zangara, J. Henshaw, A. Ajoy, R.H. Acosta, J.A. Reimer, A. Pines, C.A. Meriles, Optically pumped spin polarization as a probe of many-body thermalization, Sci. Adv. 6 (2020) eaaz6986.
[33] L.B. Casabianca, A.I. Shames, A.M. Panich, O. Shenderova, L. Frydman, Factors affecting dnp nmr in polycrystalline diamond samples, J. Phys. Chem. C 115 (2011) 19041.
[34] G. Kwiatkowski, F. Jähnig, J. Steinhauser, P. Wespi, M. Ernst, S. Kozerke, Direct hyperpolarization of micro-and nanodiamonds for bioimaging applications–considerations on particle size, functionalization and polarization loss, J. Magn. Reson. 286 (2018) 42.
[35] M. Gierth, V. Krespach, A.I. Shames, P. Raghavan, E. Druga, N. Nunn, M. Torelli, R. Nirodi, S. Le, R. Zhao, et al., Enhanced optical 13c hyperpolarization in diamond treated by high-temperature rapid thermal annealing, Adv. Quantum Technol. 3 (2020) 2000050.
[36] P.R. Zangara, S. Dhomkar, A. Ajoy, K. Liu, R. Nazaryan, D. Pagliero, D. Suter, J.A. Reimer, A. Pines, C.A. Meriles, Dynamics of frequency-swept nuclear spin optical pumping in powdered diamond at low magnetic fields, Proc. Nat. Acad. Sci. (2019) 201811994.
[37] A. Henstra, P. Dirksen, J. Schmidt, W. Wenckebach, Nuclear spin orientation via electron spin locking (novel), J. Mag. Res. 77 (1988) 389.
[38] A. Henstra, W.T. Wenckebach, Dynamic nuclear polarisation via the integrated solid effect i: theory, Noop Mol. Phys. 112 (2014) 1761.
[39] K. Tateishi, M. Negoro, S. Nishida, A. Kagawa, Y. Morita, M. Kitagawa, Room temperature hyperpolarization of nuclear spins in bulk, Proc. Nat. Acad. Sci. 111 (2014) 7527.
[40] D.E. Waddington, M. Sarracanie, H. Zhang, N. Salameh, D.R. Glenn, E. Rej, T. Gaebel, T. Boele, R.L. Walsworth, D.J. Reilly, et al., Nanodiamond-enhanced mri via in situ hyperpolarization, Nat. Commun. 8 (2017) 15118.
[41] D.E. Waddington, T. Boele, E. Rej, D.R. McCamey, N.J. King, T. Gaebel, D.J. Reilly, Phase-encoded hyperpolarized nanodiamond for magnetic resonance imaging, Sci. Rep. 9 (2019) 5950.
[42] X. Lv, J. Walton, E. Druga, F. Wang, A. Aguilar, T. McKnelly, R. Nazaryan, L. Wu, O. Shenderova, D. Vigneron, et al., High contrast dual-mode optical and 13c magnetic resonance imaging in diamond particles, arXiv preprint arXiv:1909.08064 (2019).